OVERVIEW OF DEEP STRUCTURE USING MICROSEISMICITY AT WAIRAKEI

Fabian Sepulveda[1], Jennifer Andrews[2], Mark Alvarez[2], Ted Montague[1] and Warren Mannington[1]

[1]Contact Energy Limited, Wairakei Power Station, SH1, Taupo, New Zealand

[2]Institute of Earth Science and Engineering, Auckland, New Zealand

fabian.sepulveda@contactenergy.co.nz

Keywords: *microseismicity, Wairakei, 3D seismic energy, upflow, seismic-aseismic transition, BDTZ.*

ABSTRACT

The Wairakei Seismic Network collects high spatial resolution microseismic data from thirteen downhole seismometers with depths ranging from ca. 65 m to 1,400 m. This paper examines statistical and spatial characteristics of 5,649 events recorded from March 2009-April 2013. In order to assist spatial analysis, three-dimensional, continuous numeric models of seismic energy are developed. The results show that microseismicity can improve reservoir models by constraining the depth of fluid circulation, by defining deep upflow zones, and locating horizons of higher fracture permeability.

1. INTRODUCTION

1.1 The Wairakei Geothermal Field

The Wairakei geothermal field started commercial production of electricity in 1958. With the commissioning of the Te Mihi Power Station scheduled for the second half of 2013, the installed capacity of Wairakei will total 375 MWe, sourced from Te Mihi (155 MWe), Wairakei (170 MWe) and Poihipi (50 MWe) power stations. Total output is limited by resource consents to approximately 333 MWe.

Early production of Wairakei centred in the Eastern Borefield (EBF) and progressively shifted to the Western Borefield (WBF; Figure 1). As of 2003, production drilling concentrated in the Te Mihi area (Figure 1). For more details on recent resource developments, readers can refer to Bixley et al. (2009).

Large scale injection started at Wairakei during the mid 90's (Otupu area; Figure 1). From August 2011, injection extended to the south to include the Karapiti area (Figure 1).

1.2 The Wairakei Seismic Network (WSN)

The WSN (Figure 1) represents a pioneering effort in New Zealand's geothermal industry for the collection of high quality microseismic data. During the first stage of development of the WSN (completed March 2009), nine borehole seismometers and one surface seismometer were installed, followed by a second stage of four additional borehole seismometers (completed early 2013). Currently, the WSN comprises 13 downhole seismometers spread across the Wairakei and Tauhara fields, with monitoring depths from ca. 65 m to 1,392 m (Table 1).

The objectives of the WSN include:

1) Provide support to field management and drilling strategies;

2) Monitor reservoir response to production and injection

The WSN runs independently from a seismic network operated by GNS Science (GNS) for Contact Energy (GNS monitoring sites shown in Figure 1). The objective of the GNS network is to comply with seismic hazard monitoring requirements under Wairakei and Tauhara resource consent conditions. During late 2012, station THEQ02 (Stage II of the WSN; Table 1) became the first downhole station to be shared by both GNS and WSN networks. Data collected by the GNS network is not discussed in this paper.

Table 1: WSN borehole seismic stations. mRL = meters relative to sea level; mGL = meters relative to ground level

Station	Elevation [mRL]	Sensor Depth [mGL]	Stage	Location
THEQ01	415	80	I	Infield
WKEQ02	462	80	I	Infield
WKEQ03	531	80	I	Infield
WKEQ04	451	80	I	Infield
WKM09	381	99	I	Infield
WK313	344	1392	I	Outfield
WKEQ05	483	156	I	Outfield
WKEQ06	526	154	I	Outfield
WKEQ08	514	120	I	Outfield
WKEQ07	507	65	I and II	Infield
THEQ02	468	85	II	Infield
WK402	426	1194	II	Outfield
WKEQ09	598	80	II	Outfield

2. DATA ANALYSIS

2.1 Event location

The Institute of Earth Science and Engineering (IESE) currently operates the WSN and process microseismic data for Contact Energy. Each WSN seismic station is equipped with a stand-alone (i.e. self-powered) data acquisition system and connected to a hybrid radio-cell phone telemetry system, which transmit data to a central information facility at Wairakei. To enable real-time analysis, Contact and IESE are currently working on a virtual link between Wairakei and IESE's office in Auckland.

Data are routinely recorded at high sampling rate (i.e. 200 samples per second) and processed for hypocentre locations using HYPOINVERSE-2000 (Klein, 2002), assuming a 1-D velocity model, optimised following the approach of Sambridge and Drijkoningen (1992). The velocities are generally consistent with those determined for the area by Stern & Bension (2011) from wide-angle reflection data, except for a slightly lower velocity in the depth range 3 to 6 km.

Over the period March 2009-April 2013, 5649 events were detected. Following location, moment magnitudes (M_w) are calculated from seismic energy as follows:

$$M_w = \frac{Log(M_o)+A}{B} \quad (1)$$

(Thatcher and Hanks, 1973) where M_o is seismic moment, A = -17.21 and B = 0.9825, with constants A and B adjusted empirically.

2.2 Microseismic domains

The *xyz* positional accuracy for each hypocentre locations depends on the event's location relative to the WSN array of seismic stations (Table 1). As an approximation, events occurring within the area of coverage of the WSN (Figure 1) tend to be located with higher spatial accuracy than events outside such area of coverage. Table 2 summarizes the estimated spatial errors and quality classes for events recorded until April 2013.

Table 2: Statistics of microseismic data. ERH = estimated horizontal error; ERZ = estimated vertical error; Mag = magnitude. All spatial errors in km.

Item	Quality class			
	A	B	C	D
Average of ERH	0.12	0.18	0.49	3.25
Average of ERZ	0.18	0.31	0.96	6.75
Min of Mag	-0.1	-0.6	-0.8	-1.2
Max of Mag	3.1	3.7	3.9	3.4
Min of Depth	0.0	0.0	0.0	0.0
Max of Depth	6.6	14.8	21.1	40.3

Infield events, defined as those events within the inner resistivity boundary (Figure 1), correspond closely to quality classes A and B (2,235 events or 39.6% of the population). A- and B-type events are shown in cross section for reference in Figure 2. At depths greater than 5 km, A- and B-type events cluster along a westerly dipping, ENE-WSW trending planar feature, informally referred to as *Te Mihi-Poihipi* Fault. Further details on this and other structural features can be found in section 2.3.

The infield area encompasses both production and injection areas (Figure 1). For the purpose of statistical analysis of infield and outfield event distribution with depth (section 2.3 below), we segregated the population of microseismic events into four spatial domains (displayed in Figure 3) based on closeness to field boundary and injection areas:

1) Green Domain: infield events predominately in or near injection zones;
2) Red Domain: infield events far from injection zones;
3) Yellow Domain: outfield events near injection areas (from either Wairakei or neighbouring Rotokawa field); and
4) Blue Domain: outfield events far from injection areas;

A straight line is adopted as the divide between Red and Green domains (Figure 3). This boundary is a simple, effective and practical approach to distinguish infield areas with high likelihood of induced microseismicity (i.e. Green Domain) from infield areas with low likelihood of microseismicity (i.e. Red Domain), assuming increased likelihood of shallow induced microseismicity within 1 km of injection wells.

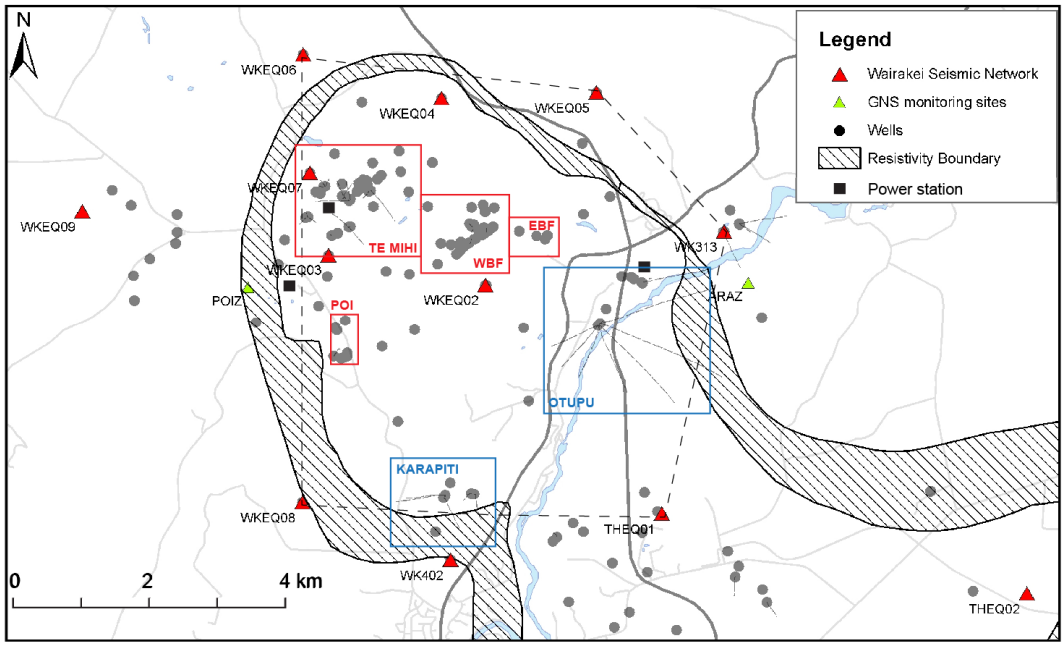

Figure 1: Map of the Wairakei Geothermal Field and WSN, showing production (Te Mihi, EBF, WBF and POI = Poihipi) and injection areas in red and blue rectangles, respectively. Dashed line is an approximate indication of the area of coverage of the WSN (first stage of development). Stations added during the second stage of development: WKEQ09, WK402, WKEQ07 (deepening) and THEQ02.

2.3 Statistical analysis: frequency versus depth

We plotted normalized event frequency with depth for different microseismic domains (Figure 4). The results show that microseismic activity declines sharply at depths greater than 6 km for all domains. We infer that this frequency decline reflects proximity to the brittle-ductile transition zone (BDTZ). In order to avoid confusion between our terminology and terms used in the literature (e.g. "seismic-aseismic", "brittle-plastic", "seismogenic zone", etc.), we define: the depth of seismic-aseismic transition as the cut-off depth above which 95% of microseismicity occurs, noted $d_{95\%}$ (e.g. Rolandone et al., 2004); the base of the seismogenic zone as $d_{99\%}$; and the BDTZ as a depth interval between $d_{95\%}$ and $d_{99\%}$ percentiles. The relevance of the BDTZ is that it outlines the base of hydrothermal fluid circulation (i.e. permeability bottom boundary). As shown by Kissling et al. (2010), a potential application of the BDTZ is its use as input parameter for numeric models of fluid circulation of the Taupo Volcanic Zone (TVZ).

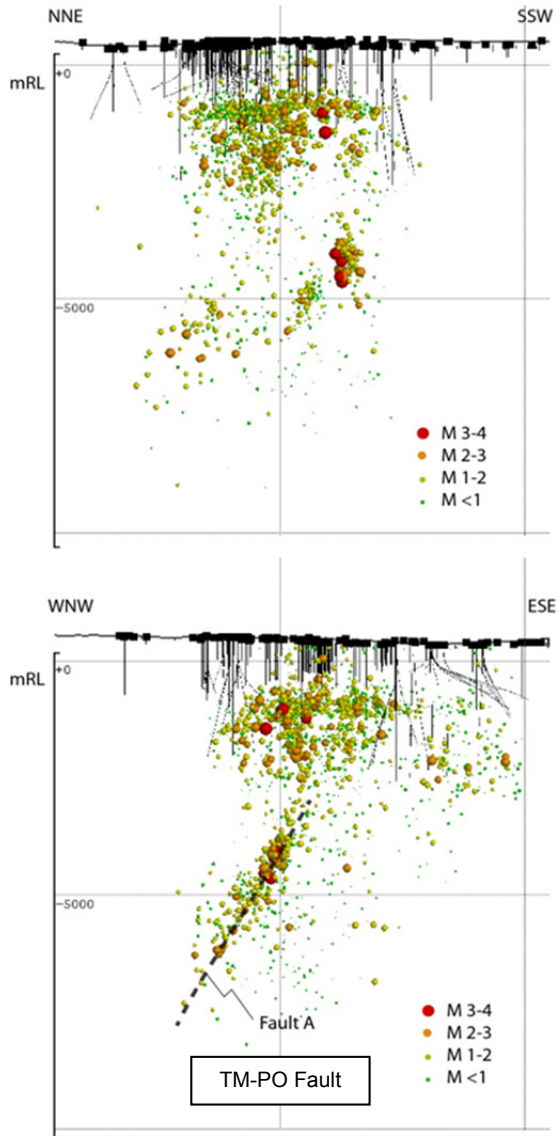

Figure 2: Cross sections of microseismicity (high quality, A- and B-type events only). Events coloured and sized by magnitude. TM-PO = Te Mihi-Poihipi Fault (see section 2.4 and 3 for discussion)

The values of $d_{95\%}$ and $d_{99\%}$ can be affected by:

1) Completeness of the seismic record. The period March 2009-April 2013 used here is regarded statistically representative for the purpose of estimation of $d_{95\%}$ and $d_{99\%}$.
2) Precision of the hypocentre locations. Based on the close correlation between A- and B-type events (mostly confined to within the area of coverage in Figure 1) and infield events, infield $d_{95\%}$ and $d_{99\%}$ percentiles can be assumed to be more accurate than outfield percentiles.
3) Microseismic domains. Looking at individual domains (Figure 4), the infield BDTZ (Figures 4-B and 4-C) rises higher relative to the outfield BDTZ (Figures 4-D and 4-E). This highlights the potential utility of the BDTZ as a geothermometer (e.g., if $d_{95\%}$ is used as a proxy of a particular isotherm) with a higher infield BDTZ consistent with a shallow heat source. Also, all infield data (Figure 4-B; Green + Red domains in Figure 2) show a shallower BDTZ relative to infield data far from injection areas (Figure 4-C; Red domain in Figure 2). This supports the hypothesis of the Green Domain having a greater proportion of shallow induced microseismicity relative to the whole infield region (Figure 2). Similarly, a higher proportion of induced seismicity can be invoked to explain the shallower BDTZ of all outfield data (Figure 4-D) relative to outfield data far from injection areas (Figure 4-E).

Based on the observations above, "near-natural-state" (i.e. far from injection areas) $d_{95\%}$ and $d_{99\%}$ percentiles are approximated using Red and Blue populations (Figure 2). This is to say: infield $d_{95\%} = 6.5 \pm 0.5$ km; infield $d_{99\%} = 8.5 \pm 0.5$ km; outfield $d_{95\%} = 10.2 \pm 1.0$ km; outfield $d_{99\%} = 16.4 \pm 2.0$ km.

The frequency-depth profiles also reveal an apparent microseismicity "gap" in the 4-5 km depth interval (Figure 4). Currently, it is difficult to prove this decrease is statistically significant or to propose a mechanism to explain its existence.

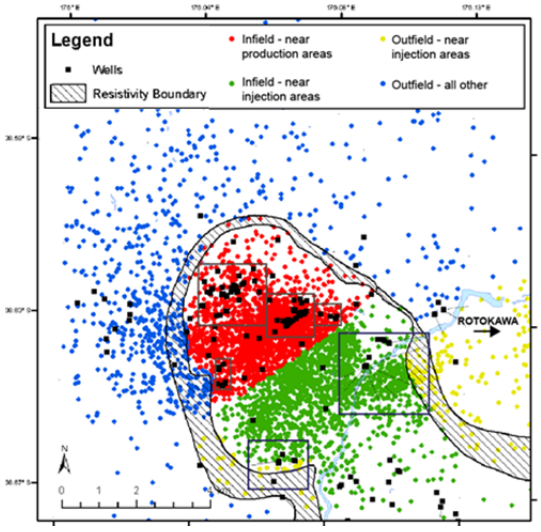

Figure 3: Microseismicity at Wairakei for period March 2009-April 2013 and microseismic domains (see section 2.2 for further explanation). Production and injection areas shown in rectangles as in Figure 1.

-

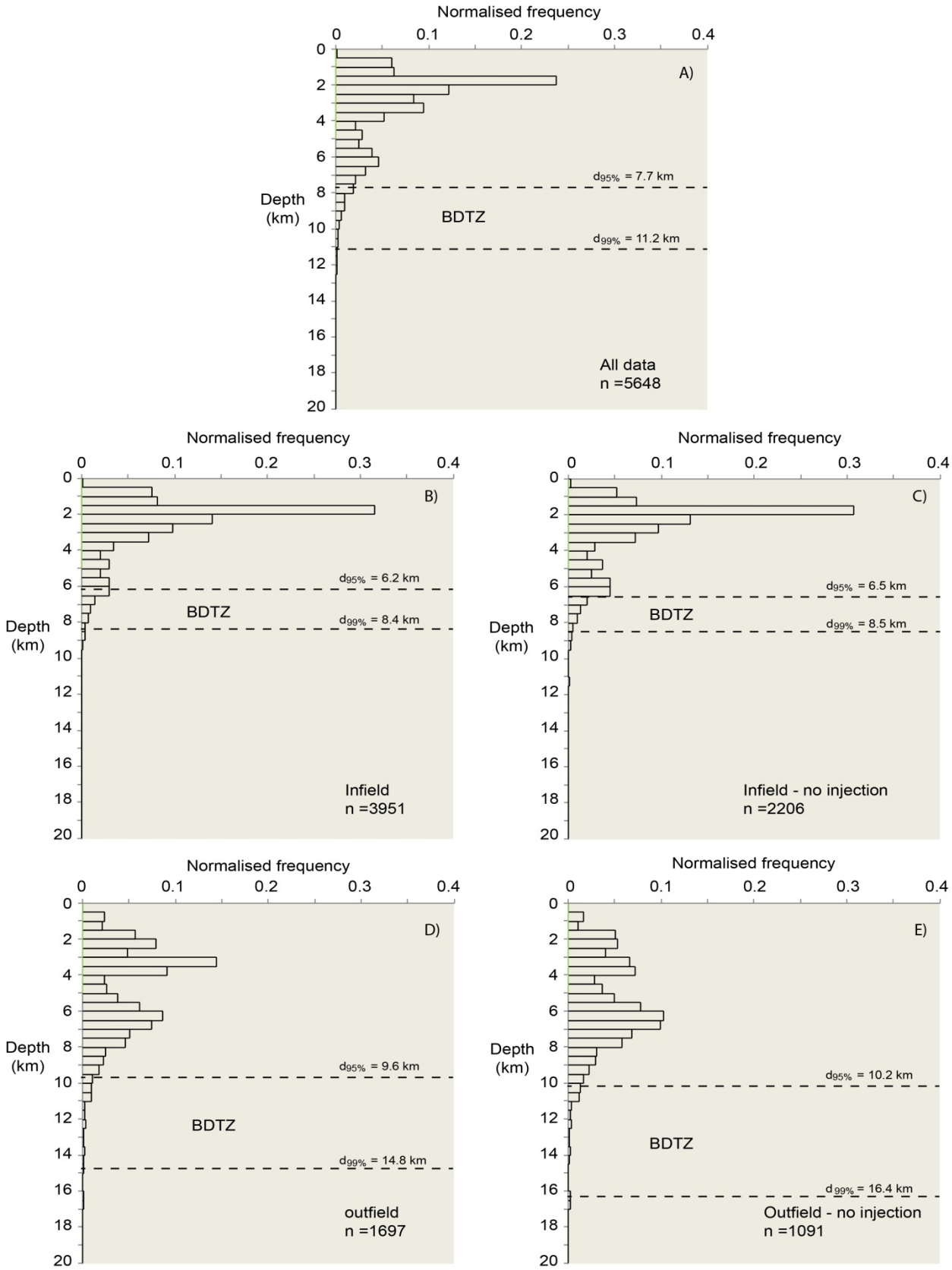

Figure 4: Histograms of normalised frequency with depth for different microseismic domains (see Figure 3 and section 2.2 for further explanation), showing BDTZ as defined by $d_{95\%}$ and $d_{99\%}$ percentiles.

2.4 Numeric models of seismic energy

Recent studies (e.g. Geiser et al., 2012) prove continuous numeric models of seismic energy useful for analysis and visualisation of seismic data, as an alternative approach to conventional mapping of xyz hypocentre locations (such as in Figure 2). Using an analogue concept to that of Geiser et al. (2012), we compute three-dimensional (3D) numeric models of log of cumulative seismic moment (referred to as LogM_{oc} here) to support spatial analysis. The modelling of LogM_{oc} involved discretisation of 3D space into a regular grid of 150 m spatial resolution, which was then populated with LogM_{oc} values, and input into Leapfrog 3D software package for numeric modelling.

A number of major structural features can be identified using continuous models of LogM_{oc} (Figure 5). In order to facilitate description of these features, these are informally labelled, from bottom to top, as *Te Mihi-Poihipi* (TM-PO) Fault (Figures 2, 5-A and 5-B), *Western* Fault (Figure 5-B), *Central* Fault (Figure 5-D), *Karapiti-Otupu* (KR-OT) Fault (Figure 5-D) and *Alum Lakes* (AL) Fault (Figure 5-E). Some of these features are shown in cross section view (Figure 6), superimposed on a 3D geological model of Wairakei developed by GNS Science for Contact Energy. No attempt has been made in this paper to correlate the interpreted structures with surface faults (e.g. GNS Active Fault Database).

3. DISCUSSION

Based on the close correlation between shallow seismic energy anomalies (~ 1.5 km depth; Figure 5-F) and the resistivity boundary, we postulate that shallow microseismic activity effectively outlines the lateral extent of the modern geothermal system. Deep microseismicity (>5 km depth) tends to concentrate near the north-western boundary (as suggested by the resistivity boundary) suggesting changing field boundaries with depth.

The *TM-PO* Fault (Figures 5-A, 5-B and 6) is interpreted as the deep manifestation of the upflow of the Wairakei system. The base of the hypothesised upflow, located at 6.5-8.5 km (Figure 4-C), is used as a proxy for the maximum depth of fluid circulation under Wairakei. Although the BDTZ boundaries could be potentially used as a geothermometer, with some authors suggesting a temperature range of 370-400°C for the BDTZ (e.g. Fournier, 1999), there remains some uncertainty as to the absolute temperatures prevailing at the proposed BDTZ.

Both *Western* and *Central* faults (Figures 5-B and 5-D, respectively) strike nearly perpendicular to the NE-SW structural trend of the TVZ. Rowland and Sibson (2004) hypothesized the existence of NW-SE trending structures in the TVZ corresponding to accommodation zones which could enhance permeability. A potential implication of this study is that oblique structures do constitute permeability paths at Wairakei in addition to the NE-SW trending structures.

The *AL* Fault (Figure 5-D and Figure 6) is interpreted as a shallower (1-3 km depth) manifestation of one of the possible upflows of the Wairakei geothermal system. The Alum Lakes thermal area (south of Te Mihi and south-west of WBF; Figure 1) remains relatively unexplored; WK121 was drilled into Wairakei Ignimbrite (for a detailed description of this and other geological units, refer to Bignall et al., 2010) in the vicinity of the *AL* fault and recorded the second highest temperature at Wairakei (267°C) although with poor permeability.

The highest temperature on record at Wairakei is 272°C and measured in well WK268, drilled during mid 2012 into Karapiti 2B rhyolite in Te Mihi area (Karapiti 2B shown in Figure 6). It is interesting to note that "microseismic plumes", as those observed underneath Alum Lakes area, are not evident underneath Karapiti 2B rhyolite (Figure 6).

The *KR-OT* fault (Figure 5-C) extends over a depth range of 2-3 km and it is slightly obtuse to the regional NE-SW trend of the TVZ. The *KR-OT* fault is not imaged in the immediate perimeter of the injection areas but some distance north of Karapiti injection wells, and some distance south (and deeper) of most Otupu injection wells. The offset of *KR-OT* fault with respect to injection areas gives insight into the fluid path of injection fluids suggesting a mixed conduit-barrier behaviour of the *KR-OT* fault.

While a range of processes may trigger microseismicity in active high-temperature geothermal fields, including fluid pressure increase and/or thermal rock contraction (e.g. injection areas), microseismicity is thought to be ultimately the expression of "fracture-permeability" (associated with shear faulting). In this context, the close spatial correlation between laterally extensive microseismicity and Wairakei Ignimbrite (Figure 6) points to "stratigraphically-controlled" microseismicity. We hypothesise that favourable conditions in Wairakei Ignimbrite promoting microseismicity may include: 1) localised, low rock cohesive strength associated with pre-fractured nature of welded ignimbrites (e.g. columnar jointing; Wohletz, 2006); 2) favourable orientation of such sub-vertical joints to reactivation under extension stress regime (see Sibson (1998) for details on fault reactivation analysis); 3) localised increase in fluid pressure promoted by self-sealed permeability following hydrothermal mineral precipitation.

4. CONCLUSIONS AND FUTURE WORK

Microseismicity data collected to date from the WSN provides unprecedented high spatial resolution data for characterisation of deep structures at Wairakei. The contributions of this paper area summarised as follows: 1) quantitative characterisation of base of recharge zone at Wairakei and outfield areas (BDTZ); 2) imaging of potential upflow(s) of the Wairakei geothermal system and horizons of high fracture permeability; 3) introduction of 3D numeric models of seismic energy as a tool for analysis of high resolution microseismic data.

The potential of microseismicity as an exploration and monitoring tool is significant and further work on the fronts of joint geophysical imaging and advanced microseismic data analysis (e.g. tomography, focal mechanism, shear-wave splitting, etc) are anticipated.

ACKNOWLEDGEMENTS

The authors would like to thank Contact Energy Limited for permission to publish data. Also we would like to acknowledge Mike Hasting for his collaboration during the first stage of development of the WSN. Thanks are extended to Paul Bixley for useful comments to the manuscript.

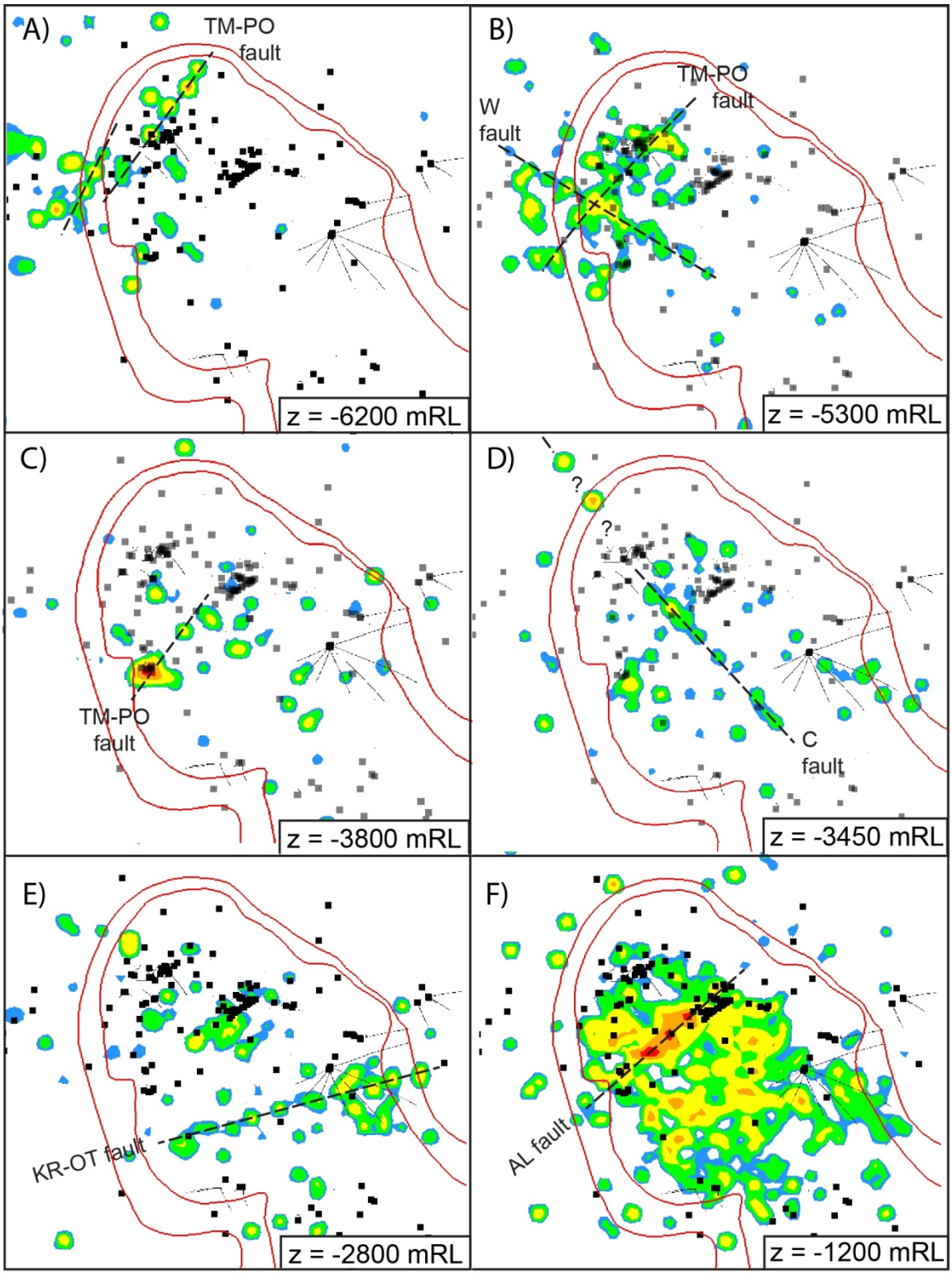

Figure 5: Maps of LogMoC highlighting some interpreted structural features: TM-PO = Te Mihi-Poihipi Fault; KR-OT = Karapiti-Otupu Fault; AL = Alum Lakes Fault. Colour scale is relative scale, with blue = lower and red = higher LogMoC values.

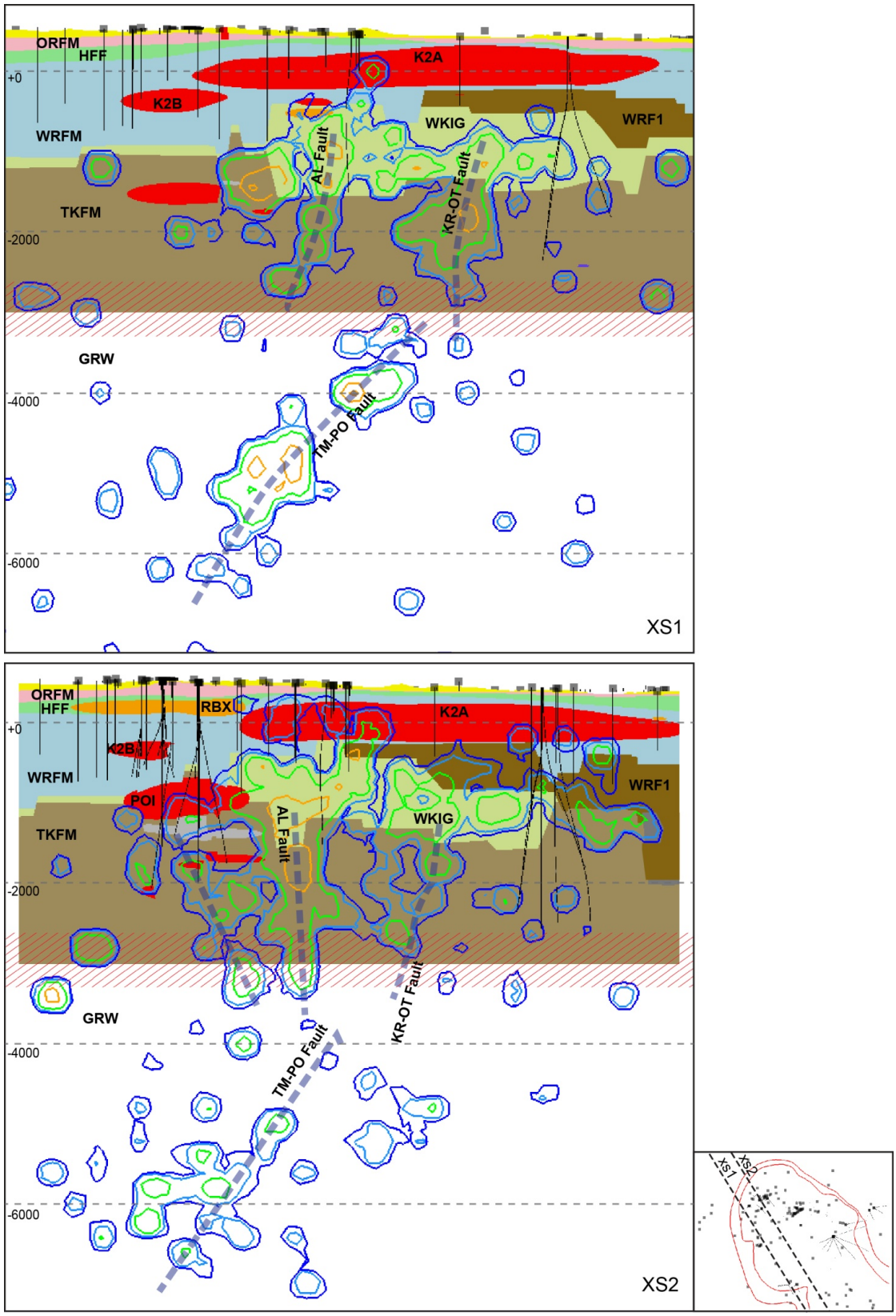

Figure 6: Geological cross sections xs1 and xs2 from NW (left) to SE (right), with contours of LogMoC (relative colour scale, as in Figure 5) and some interpreted structural features (dashed lines; key as in Figure 5). Geological unit key: ORFM = Oruanui Formation; HFF = Huka Falls Formation; WRFM = Waiora; WRF1 = Waiora Formation 1; WKIG = Wairakei Ignimbrite; TKFM = Tahorakuri Formation; GRW = Torlesse Greywacke; K2A = Karapiti 2A Rhyolite; K2B = Karapiti 2B Rhyolite. For details on geology, see Bignall et al. (2010). Red hatched area represents expected transition from TKFM to GRW (interpreted from residual gravity anomalies).

REFERENCES

Bignall, G., Milicich, S., Ramirez, E., Rosenberg, M., Kilgour, G., and Rae, A. Geology of the Wairakei-Tauhara Geothermal System, New Zealand. Proceedings World Geothermal Congress 2010, Bali, Indonesia, 25-29 April (2010).

Bixley, P. B, Clotworthy, A. W., Mannington, W. I. Evolution of the Wairakei geothermal reservoir during 50 years of production. Geothermics, 38, 145–154 (2009)

Fournier, R. O., 1999. Hydrothermal Processes Related to Movement of Fluid from Plastic into Brittle Rock in the Magmatic-Epithermal environment. Economic Geology, 94, 1193-1211 (1999).

Geiser, P., Lacazette, A. and Vermilye, J.: Beyond 'dots in a box': an empirical view of reservoir permeability with tomographic fracture imaging. First Break, 30, 63-69 (2012).

Kissling, W. M., Ellis, S., Charpentier, F. and Bibby, H. Large Scale Convective Flows with a Brittle-Ductile Transition. Proceedings World Geothermal Congress 2010, Bali, Indonesia, 25-29 April (2010).

Klein, F.W.: User's Guide to HYPOINVERSE-2000, a Fortran Program to Solve for Earthquake Locations and Magnitudes. USGS Open File Report 02-171, Version 1.0 (2002).

Rolandone, F., Burgmann, R. and Nadeau, R. M. The evolution of the seismic-aseismic transition during the earthquake cycle: Constraints from the time-dependent depth distribution of aftershocks. Geophysical Research Letters, 31, doi: 10.1029/2004GL021379 (2004)

Rowland, J. V. and Sibson., R. H. Structural controls on hydrothermal flow in a segmented rift system, Taupo Volcanic Zone, New Zealand. Geofluids, 4, 259–283 (2004)

Sambridge, M. and Drijkoningen, G. Genetic algorithms in seismic waveform inversion. Geophys. J. Int., 109, 323-342 (1992).

Sibson, R., H. Structural permeability of fluid-driven fault-fracture meshes. Journal of Structural Geology, vol 18, p 1031-1042 (1998).

Stern, T. and Benson, A. Wide-angle seismic imaging beneath an andesitic arc: Central North Island, New Zealand. J. Geophys., Res, 116, B09308 (2011).

Thatcher, W. and Hanks, T. C. Source parameters of southern California earthquakes. J. Geophys. Res, 78, 8547-8576 (1973).

Wohletz, K. Fractures in welded tuff. Geological Society of America, Special Paper 408, Chapter 2.3 (2006).